Nano Research

ISSN 1998-0124 CN 11-5974/O4
https://doi.org/10.1007/s12274-020-2876-8

Research Article

Rationally designed synthesis of bright $AgInS_2$/ZnS quantum dots with emission control

José X. Soares[1], K. David Wegner[2], David S. M. Ribeiro[1], Armindo Melo[3], Ines Häusler[4], João L. M. Santos[1], and Ute Resch-Genger[2] (✉)

[1] *LAQV-REQUIMTE, Department of Chemical Sciences, Laboratory of Applied Chemistry, Faculty of Pharmacy, University of Porto, Rua de Jorge Viterbo Ferreira, 228, Porto, 4050-313, Portugal*
[2] *Federal Institute for Materials Research and Testing (BAM), Division Biophotonics, Richard-Willstaetter-Strasse 11, 12489 Berlin, Germany*
[3] *LAQV-REQUIMTE, Laboratório de Bromatologia e Hidrologia, Departamento de Ciências Químicas, Faculdade de Farmácia da Universidade do Porto, Rua de Jorge Viterbo Ferreira, 228, Porto, 4050-313, Portugal*
[4] *Technische Universität Berlin, Institut für Optik und Atomare Physik, Straße des 17. Juni 135, 10623 Berlin, Germany*

Received: 26 August 2019 / **Revised:** 11 May 2020 / **Accepted:** 13 May 2020

ABSTRACT

In the blossoming field of Cd-free semiconductor quantum dots (QDs), ternary I–III–VI QDs have received increasing attention due to the ease of the environmentally friendly synthesis of high-quality materials in water, their high photoluminescence (PL) quantum yields (QYs) in the red and near infrared (NIR) region, and their inherently low toxicity. Moreover, their oxygen-insensitive long PL lifetimes of up to several hundreds of nanoseconds close a gap for applications exploiting the compound-specific parameter PL lifetime. To overcome the lack of reproducible synthetic methodologies and to enable a design-based control of their PL properties, we assessed and modelled the synthesis of high-quality MPA-capped $AgInS_2$/ZnS (AIS/ZnS) QDs. Systematically refined parameters included reaction time, temperature, Ag:In ratio, S:In ratio, Zn:In ratio, MPA:In ratio, and pH using a design-of-experiment approach. Guidance for the optimization was provided by mathematical models developed for the application-relevant PL parameters, maximum PL wavelength, QY, and PL lifetime as well as the elemental composition in terms of Ag:In:Zn ratio. With these experimental data-based models, MPA:In and Ag:In ratios and pH values were identified as the most important synthesis parameters for PL control and an insight into the connection of these parameters could be gained. Subsequently, the experimental conditions to synthetize QDs with tunable emission and high QY were predicted. The excellent agreement between the predicted and experimentally found PL features confirmed the reliability of our methodology for the rational design of high quality AIS/ZnS QDs with defined PL features. This approach can be straightforwardly extended to other ternary and quaternary QDs and to doped QDs.

KEYWORDS

quantum dot, core/shell nanoparticle, silver indium sulfide, microwave-assisted synthesis, design of experiment, photoluminescence

1 Introduction

Cd-free ternary I–III–VI semiconductor quantum dots (QDs) have emerged as promising alternatives for nanocrystalline emitters that can circumvent the inherent drawback of II–VI and IV–VI binary semiconductor QDs, namely the presence of toxic constituents such as Cd, Hg or Pb, and the lack of environmentally friendly synthetic routes for high quality III/V QDs like InP [1–5]. Among these ternary QDs, Cu–In-S (CIS) and Ag–In–S (AIS) QDs are particularly interesting [2, 6, 7]. Their attractive photoluminescence (PL) properties include high PL quantum yields (QYs) ≥ 50% in the entire visible to near infrared (NIR) region from about 400 nm to about 1,000 nm after passivation with e.g., a ZnS shell [8–10]. Other interesting features of these ternary QDs, that also show size confinement effects [11], are broad PL bands with full width at half-maximum (FWHM) of more than 100 nm in this wavelength region, which only slightly overlap with the rather unstructured absorption spectrum lacking the sharp first excitonic feature of II/VI and III/V QDs [12–14]. Moreover, they show long PL lifetimes of several hundred nanoseconds, which are not sensitive to the presence of oxygen.

The ternary QDs emission features, ascribed to either the radiative recombination of donor–acceptor pairs [15, 16], a self-trapped exciton model [17], the recombination of a localized hole with a conduction band electron as derived for CIS QDs [18] or a combination of these models [19], can provide the basis for many future applications of CIS and AIS QDs. Although the broad PL spectra are not ideal for some multiplexing applications, they can be advantageous, e.g., for the construction of sensor systems, solid state lighting (light emitting diodes) [10, 20], photovoltaics (photovoltaic cells [21]; light-harvesting systems/solar concentrators [22]), photocatalysis [23, 24], and luminescent probes for bioimaging [25–27].

From a chemical point of view, the most prominent characteristic of CIS and AIS QDs is their compositional and structural versatility, as they are able to accommodate non-stoichiometric ratios of their constituents and can have different

Address correspondence to ute.resch@bam.de

crystal structures (orthorhombic, tetragonal) [15, 28]. However, this versatility also represents an additional challenge for the development and optimization of synthetic methodologies to control the size, shape, and surface composition of these QDs [29]. Challenges in the synthesis of CIS and AIS QDs arise from the different reactivity of the constituting metal ions as a result of their distinct hard and soft Lewis acid and base (HSAB) character [3]. For example, in the case of AIS QDs, which are in the focus of this article, In(III) is a "hard" while Ag(I) is a "soft" Lewis acid [30]. Consequently, the synthesis of AIS QDs requires a non-stoichiometric ratio of the metal ions with indium being used in excess [3]. The precursor ratio also considerably influences the PL properties of the resulting AIS QDs [11, 30–32]. Additionally, the deposited ZnS shell often does not merely play a protective role but can also initiate a cation exchange (CE) between the zinc ions added during the shelling procedure and the metal ions forming the QD core. This can lead to alloy formation, yielding a hybrid between a ternary and a quaternary nanomaterial [32–35]. Seeking a balance between the different cation reactivities is a demanding task, independent of the chosen synthetic route, e.g., hot-injection or aqueous-based synthesis. The synthesis of high quality QDs in water, which is increasingly preferred to meet environmental concerns, presents an additional challenge. Besides their role in colloid stabilization, typically employed small water-soluble thiol ligands such as 3-mercaptopropionic acid (MPA) form complexes with Ag(I) [36], In(III) [37], and Zn(II) [36], with the complex stoichiometry depending on ligand concentration [38]. Therefore, the initially used or so-called feeding thiol:In(III) ratio is also important for balancing the thiol binding strength to the different metal cations present in the reaction mixture [30]. For all aqueous syntheses, pH is a crucial parameter, as it controls the thiol protonation state and the formation of metal hydroxides, present either as soluble complexes or as precipitates [3]. Bearing in mind that the hydroxide ion is a typical hard base, the effective concentration of free indium(III), for example, can largely depend on the pH. Other synthetic parameters affecting the PL features of the resulting AIS/ZnS QDs are temperature and reaction time during the AIS core and the ZnS shell synthesis. For the preparation of high quality AIS/ZnS QDs in water, microwave (MW)-assisted methods are very attractive. These methods have been widely explored for the synthesis of water-soluble binary II–VI QDs [39–43], but were scarcely used for AIS QDs until now [44–48]. This is related to the efficient absorption of MW irradiation by the solvent water and the metal ion precursors. Moreover, MW synthesizers enable a rapid and homogeneous increase in temperature, which reduces the possibility of a temperature gradient in the reaction mixture, consequently yielding a more efficient, uniform, and controlled nucleation and growth of the nanoparticles [49, 50]. MW heating also expands the reaction temperature range due to water superheating, allowing reactions to be performed above its boiling point [51], and enabling automation.

Contrary to binary II–VI QDs where the emission color can be easily tuned by changing the reaction time, the manifold of parameters affecting the synthesis of ternary QDs, like AIS nanocrystals (NCs), and their unknown interplay render the rational design of AIS QDs almost impossible. A useful tool to rationally guide the optimization of complex processes is the design of experiment (DoE) approach. Its cornerstone is the assumption that the outcome of a reaction can be described by a mathematical equation [52, 53]. Based on the experimental data, a mathematical model can be established to describe the studied system and, consequently, to predict the experimental conditions, which provide the optimum outcome [54–56]. This encouraged us to study the applicability of DoE for the rationally driven MW-assisted synthesis of MPA-capped AIS/ZnS QDs in water with optimum PL features. Subsequently, we performed a "top-down" optimization, where the reaction parameters were systematically narrowed, guided by mathematical models developed based on our experimental data. This allowed us to predict different outcomes of the underlying reactions, that were then validated by new experiments. Consequently, a methodology was developed to rationally design high quality AIS/ZnS QDs with control over elemental composition and PL properties like emission color and PL decay kinetics and to better understand the relationship between the reaction conditions and these features.

2 Experimental

2.1 Chemicals

Silver(I) nitrate ($AgNO_3$, 99.8%, Bernd Kraft), anhydrous indium(III) chloride ($InCl_3$, 98%, abcr GmbH), 3-mercaptopropionic acid (MPA, 98%, Merck KGaA), sodium sulfide nonahydrate ($Na_2S{\cdot}9H_2O$, 98%, Acros Organics), zinc(II) nitrate hexahydrate ($Zn(NO_3)_2{\cdot}6H_2O$, 99.998%, Alfa Aesar), ammonium hydroxide solution (NH_4OH, 25%, Merck KGaA), and ethanol abs. (p.a., Chem-Lab NV) were used without further purification. All solutions were prepared using bidistilled water with a resistance not exceeding 18 MΩ·cm. $InCl_3$ was used for the synthesis as 1.0 mol·L^{-1} solution containing 0.1 mol·L^{-1} HNO_3. The remaining precursors were used as 1 mol·L^{-1} solution.

2.2 MW-assisted AIS QDs synthesis

AIS synthesis was performed using a modified procedure of the synthesis reported by Raevskaya et al. [11]. In a typical synthesis, $AgNO_3$ (0.04 mmol), MPA (1 mmol) and NH_4OH (1 mmol) were added in a 35-mL reaction vessel with 25 mL of water. $InCl_3$ (0.2 mmol) was then added dropwise and the pH was adjusted to 8.5 by the addition of small amounts of NH_4OH. Na_2S (0.5 mmol) were then added and the resulting solution was MW-heated in a CEM Discover SP® Microwave Synthesizer. An initial power output of 200 W was applied until the desired temperature of 100 °C was reached, which was maintained for 50 min. After this heating period, MPA (0.2 mmol), NH_4OH (0.2 mmol) and $Zn(NO_3)_2$ (0.2 mmol) were added to the reaction mixture, which was then heated for 30 min at 100 °C. For the precipitation of the obtained QDs, ethanol (50 mL) was added and the dispersion was centrifuged for 5 min at 10,000 RCF with a Rotina 380R centrifuge (Hettich Lab Technology), the precipitate was collected and re-dispersed in water, and the procedure was repeated two times. The obtained QDs samples were stored in amber glass vials at room temperature.

2.3 Design of the experiments

The screening of the significant synthesis parameters was done with a two-level fractional factorial design. Five variables were included in the model, with each parameter being examined at two different levels, as shown in Table 1. A 2^{5-1} fractional factorial design, composed of 16 experiments, were chosen as it provided the necessary design resolution to characterize the design space. The experimental conditions for the synthesis of highly luminescent AIS/ZnS QDs were optimized using a central composite design (CCD). The three most significant variables Ag:In ratio, MPA:In ratio, and the pH of the solution were included. CCD consisted of a 2^3-factorial design as cubic

Table 1 Reaction parameters and their lower and upper limits used for the initial optimization

Parameter	Lower value	Upper value
Ag:In ratio	0.08	0.24
S:In ratio	1	2
Zn:In ratio	1	2
MPA:In ratio	4	8
pH	8.5	10.5
Core time (min)[a]	10	60
Shell time (min)[b]	5	40
Temperature (°C)	100	140

[a]Reaction time used for the synthesis of the $AgInS_2$ core. [b]Reaction time used for the synthesis of the ZnS shell.

points, with six axial points at a distance of $\alpha = 1.682$ and five center points. Five different responses were used. The statistical analyses of the fractional factorial design and of CCD were performed with Design Expert v. 11 (Stat-Ease Inc. Minneapolis, MN, USA). The suitability and significance of the models were evaluated by analysis of variance (ANOVA) with Fisher's F test. The terms with p-value > F lower than 0.05 were considered significant. The goodness of fitting was evaluated by a Lack-of-Fit test and by adjusted-R^2 and predicted-R^2 values.

2.4 Characterization of the QDs

Elemental analysis was done using the inductively coupled plasma optical emission spectrometer (ICP-OES) SPECTRO ARCOS (SPECTRO Analytical Instruments GmbH., Kleve, Germany). The zeta potential was measured with the Zetasizer Nano ZS (Malvern Panalytical, Almelo, Netherlands). Attenuated total reflection-Fourier transform infrared (ATR-FTIR) spectra were recorded with a Perkin Elmer Frontier spectrophotometer (Waltham, MA, USA). Transmission electron microscopy (TEM) studies were performed with a scanning transmission electron microscope Fei Titan 80-300 (FEI, Hillsboro, OR, USA) at 300 kV. X-ray diffraction (XRD) measurements were done with a Rigaku Ultima IV diffractometer (Rigaku, Tokio, Japan) with Cu Kα radiation ($\lambda = 0.15406$ nm).

The spectroscopic characterization was performed with as-prepared QD solutions in standard 1.0 cm optical quartz cuvettes. The absorption spectra were recorded with a calibrated Cary 5000 spectrophotometer (Varian Inc. Palo Alto, CA, USA). The emission spectra were obtained with a FluoroMax-4 spectrofluorimeter (HORIBA Jobin Yvon GmbH, Bensheim, Germany) in standard 1.0 cm optical quartz cuvettes. The QDs were excited at $\lambda = 400$ nm, if not stated otherwise. The emission spectra were corrected with the emission correction file provided by the instrument manufacturer. The reliability of this correction file was controlled by comparison of the resulting spectra with spectrally corrected emission spectra obtained for selected samples using an FLS-920 spectrofluorometer (Edinburgh Instruments, Livingston, UK) calibrated by BAM. The spectrally corrected emission spectra were smoothed prior to the determination of the emission maxima (λ_{max}). The photoluminescence QYs were measured absolutely using a calibrated Quantaurus-QY stand-alone integrating sphere setup C11347-11 (Hamamatsu Photonics, Hamamatsu, Japan) equipped with a 150 W xenon light source, a monochromator, an integration sphere, a spectrograph and a silicon charge coupled device. Fluorescence lifetime measurements were performed with a FLS-920 fluorescence lifetime spectrometer (Edinburgh Instruments, Livingston, UK) equipped with a pulsed EPLED laser with a wavelength of 330 nm, a pulse repetition rate of 200 kHz and using time-correlated single-photon counting (TCSPC). The PL decay kinetics were measured at the emission maximum of each sample, and were recorded within 4,095 channels and collected with a constant rate of 1,000 counts·s^{-1}. The instrument response function (IRF) was measured under the same conditions with a scattering solution of non-emissive colloidal silica. The PL decays of the QDs were fitted with a multi-exponential model, see Eq. (1)

$$I(t) = \sum_n a_n e^{\left(-t/\tau_n - \frac{t}{\tau_n}\right)} \quad (1)$$

where a_n are the amplitudes and τ_n the lifetimes of the respective decaying species. These data were calculated with a reconvolution fitting procedure using the FLS-920 spectrometer software. The fit quality was evaluated from the corresponding χ^2 values. Biexponential or triexponential fits were done as the resulting χ^2 values were closer to 1 than for mono-exponential fits. The average lifetimes were calculated as an amplitude-weighted average, see Eq. (2) [57]

$$<\tau> = \frac{\sum_n A_n \tau_n}{\sum_n A_n} \quad (2)$$

where, τ_n are the lifetimes of each component and A_n the corresponding relative fractional amplitudes. Further details about the experiments are provided in the Electronic Supplementary Material (ESM).

3 Results and discussion

3.1 Parameter definition

The first step to design a methodology for the synthesis of AIS/ZnS QDs with rationally envisaged properties is the definition of the reaction parameters. We envisioned an unprecedented approach by considering all parameters, independent of their expectable importance for the outcome of the synthesis of AIS and AIS/ZnS QDs. This included the feeding ratios of Ag:In, S:In, Zn:In, and MPA:In as well as pH, time for the synthesis of the $AgInS_2$ core, time for the synthesis of the ZnS shell, and temperature. For each parameter, the working range was defined (Table 1) considering the reaction mechanism and related requirements, e.g. a suitable pH, the feeding ratios reported for similar synthetic procedures [11, 30, 32, 58], and the results from preliminary screening studies (Table S2 in the ESM).

3.2 Time and temperature optimization

The reaction time was optimized first, while the other parameters were kept constant. Subsequently, the temporal evolution of the optical properties of the AIS QDs was assessed assuming for each parameter the average value between the corresponding lower and upper limits, given in Table 1 (Ag:In ratio of 0.16; S:In ratio of 1.5; Zn:In ratio of 1.5; MPA:In ratio of 6; pH of 9.5). The reaction temperature was fixed at 100 °C, while the reaction time was varied. The PL features of the resulting QDs were used as main screening tools to evaluate QD performance. A feature typically found in the synthesis of QDs including I–III–VI ternary QDs is the increase in PL intensity with time, while the wavelength of PL emission maximum (λ_{max}) remains more or less unaffected [26, 30, 59, 60]. Additionally, samples taken at defined reaction times were also characterized with analytical methods like TEM, X-ray powder diffraction (XRD), and ICP-OES. Measurements of the zeta potential were also done as a measure for colloidal stability.

A representative absorption spectrum of our AIS QDs is shown in Fig. 1(a) underlining the previously mentioned lack of a sharp first excitonic peak and the long, so-called Urbach tail below the bandgap energy (E_g). This tail is ascribed to phonon-assisted optical transitions [61, 62]. As displayed in Fig. 1(a), the prepared AIS QDs revealed the expected Urbach tail at a wavelength of about 500 nm. The absorption spectrum, however, also showed a sharp absorption peak at 289 nm. The surprisingly pronounced structure of this absorption peak is not typical for AIS QDs and it was only found under these specific conditions. This feature was evident from the beginning of the synthesis (Fig. 1(b), 10 min) up to a reaction time of 50 min but became less pronounced for reaction times exceeding the optimum reaction time (see Fig. 1(b)). The assignment of this absorption peak at around 289 nm is not clear yet. One possible explanation could be the formation of ternary or alloyed nanoclusters intermediates, that have been reported e.g. for $Zn_xCd_{y-x}Se_y$ semiconductors [63]. The intermediate nature of these species follows immediately from the temporal course of the absorption peak at about 290 nm, as this feature eventually disappears at longer reaction times or at higher reaction temperatures (Fig. S3 in the ESM).

The formed AIS QDs displayed broad emission bands ((FWHM) of ~ 0.5 eV), see Fig. 1(c), when compared with traditional II–VI QDs. For example, the absorption and emission spectra of monodisperse hydrophobic thick shell CdSe/CdS QD in hexane with a QY close to 1 show a FWHM of the first sharp excitonic absorption maximum of about 37 meV and a FWHM of the emission band of 65 meV [64–67]. The spectral widths of the emission bands were obtained assuming a symmetric shape of the emission spectra that were only recorded up to 790 nm. The origin of the broad PL of AIS QDs has been described by different models like the donor–acceptor model [15, 16], the self-trapped exciton model [17], a free-to-bound charge carrier recombination mechanism [18, 68], and a model combining all these models recently suggested by us [19]. The PL intensity of the AIS QDs (Fig. 1(c)) and the QY values increased as function of the reaction time (Fig. 1(d)), while the maximum of the PL emission was slightly blue shifted (Fig. 1(c)). A maximum QY value of 0.24 was reached after 50 min. PL emission band also narrowed as function of the reaction time, which is attributed to annealing. Parallel performed measurements of the zeta potential revealed a drop during the reaction from –40 to –30 mV, possibly due to thiol decomposition. Nevertheless, this zeta potential is still sufficient to guarantee a good colloidal stability (Fig. 1(d)).

Time-resolved PL measurements of the AIS QDs at different reaction times always revealed complex decay kinetics. The PL

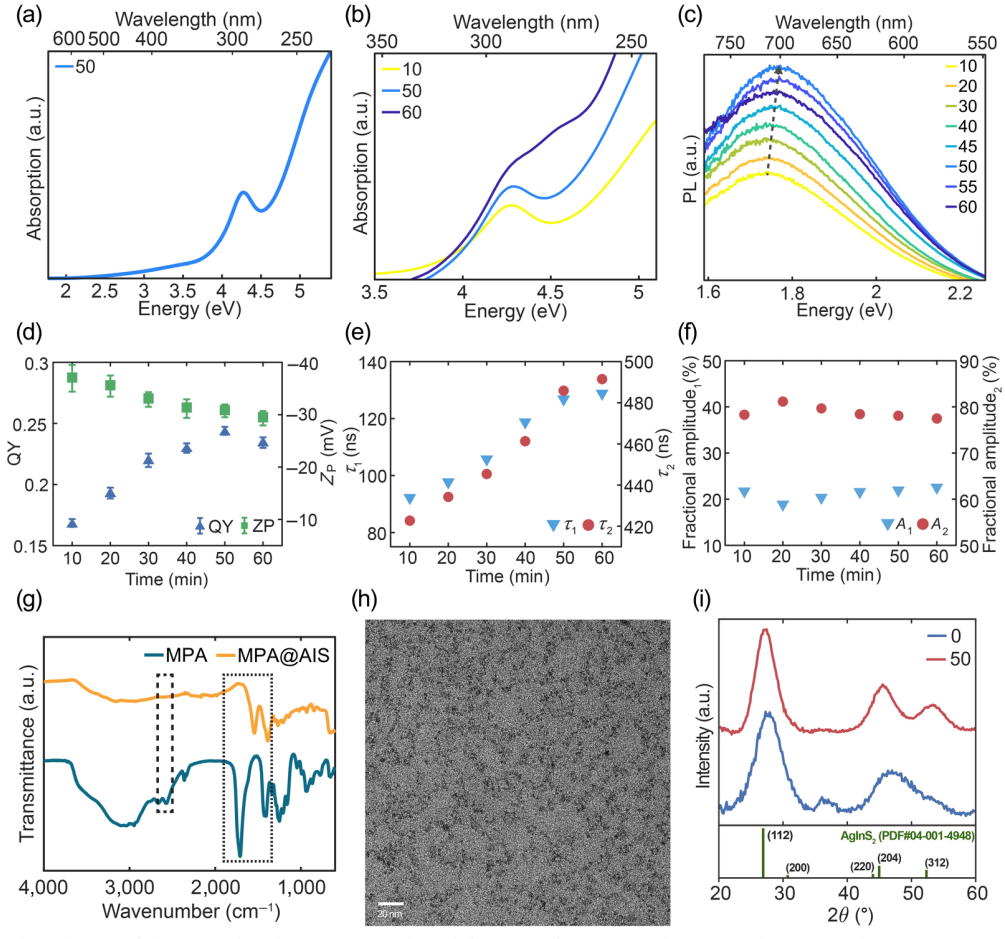

Figure 1 Temporal evolution of the optical and structure-analytical features of AIS QDs during synthesis. (a) Absorption spectra of the AIS QDs obtained after 50 min as representative absorption spectrum of AIS QDs. (b) Evolution of the absorption spectra of the AIS QDs resulting after 10 min (yellow), 50 min (blue), and 60 min (dark blue); (c) PL emission spectra; (d) QY (blue triangles) and zeta potential (green squares) of the AIS QDs as a function of reaction time. (e) PL lifetime of the short-lived component (τ_1; blue triangles) and the long-lived component (τ_2; red circles) derived from the biexponentially fitted decay curves of the AIS QDs as a function of reaction time. (f) Fractional amplitudes (in percent) of both decay components derived from the biexponentially fitted decay curves as a function of reaction time. (g) FTIR spectra of the MPA-capped AIS QDs (blue) and the ligand MPA (yellow); the dashed rectangle marks the absorption range of the SH group and the dotted rectangle the absorption range of the COO^- group. (h) Low-magnification TEM image of the AIS QDs resulting after 50 min; showing an overview of the QDs. (i) XRD diffraction pattern of the AIS QDs before heating (0 min, blue) and after 50 min of heating (50, red) in comparison to the XRD pattern of bulk chalcopyrite $AgInS_2$.

decays could satisfactorily be fitted with bi-exponential kinetics (Table S3 and Fig. S4 in the ESM), yielding a short-lived component with a fluorescence lifetime of about 110 ns and a long-lived component with a fluorescence lifetime of about 450 ns (Fig. 1(e)). These fits present, however, a simplification of the AIS photophysics and do not really imply that there are only two well defined emissive species present, but rather reflect a distribution of long-lived and short-lived species as previously described by us [19]. The observed decay kinetics and long fluorescence lifetimes of the AIS QDs exceed those of II/VI semiconductors like CdSe and CdTe, which have radiative lifetimes in the range of 20 to 40 ns [69–71]. This behavior agrees very well with the PL lifetimes of ternary AIS QDs observed by other groups and previously reported by us [19] and the PL decay kinetics of CIS QDs [29]. During the course of the reaction, the lifetimes of the short and the long decay component increased (Fig. 1(e)), while their relative fractions, referred to here as fractional amplitudes, remained constant (Fig. 1(f)).

The surface passivation of the AIS cores by the organic ligand shell was confirmed by FTIR, see Fig. 1(g). The FTIR spectrum of the MPA-capped AIS QDs revealed the presence of MPA on the QD surface as indicated by the absence of the S–H stretching vibration in the range of 2,600–2,550 cm^{-1} and the presence of the asymmetric and symmetric stretching vibrations of the COO^- group at 1,554 and 1,380 cm^{-1}. In comparison to free MPA, the MPA-capped AIS are lacking the broad and intense O–H stretching vibration and the carbonyl absorption band is shifted. This underlines the deprotonation of the carboxylic acid group in the case of MPA-stabilized AIS QDs.

TEM analysis of AIS QDs obtained at reaction times of 50 min revealed approximately tetrahedral shaped and crystalline AIS QDs with an average diameter of ca. 2.7 nm (Fig. 1(h) and Fig. S5 in the ESM). The relatively broad particle size distribution was attributed to the aqueous based synthetic route and the lack of a size-selective precipitation. TEM images obtained at different reaction times did not show a clear difference in terms of size (Fig. S5 in the ESM depicts the comparison between AIS QDs after 10 and 50 min). Although it is known that the size distribution of QDs contributes to the spectral width of the PL band, but as demonstrated, e.g. by our recently performed single-particle measurements, a relatively broad PL band is an intrinsic feature of AIS QDs [14]. Therefore, the AIS QDs particle size is not so relevant as it is for binary II–VI QDs. To assess the temporal evolution of the crystallinity of the QDs during synthesis, the XRD pattern determined for weakly fluorescent AIS QDs (data not shown), prepared without heating, were compared with those derived for brightly emissive AIS QDs obtained after heating of the reaction mixture for 50 min (Fig. 1(i)). Due to the small particle size, all XRD pattern exhibit three broad peaks at matching positions compatible with the indices for the (112), (204), and (312) planes of tetragonal chalcopyrite $AgInS_2$. The XRD peaks are shifted to larger angles compared to the bulk material. This may reflect a decrease in bond length in the AIS QDs or more likely a stoichiometry of the AIS QDs that differs from that of the bulk material. Using the Scherrer equation, the calculated average crystal size of AIS QDs was 2.3 nm, which is in accordance with TEM data. The XRD pattern of the weakly fluorescent AIS QDs prepared without heating suggests the rapid formation of quasi-crystalline QDs at room temperature, while the narrowing of the broad XRD peaks after heating indicates that during heating the QDs have grown in size and improved their crystallinity.

The elemental composition of the AIS QDs determined with ICP-OES (Fig. 2(a)) revealed a decrease in Ag:In ratio with increasing reaction time. This indicates that AIS QDs grew by incorporating more "hard" Lewis acid indium than "soft" Lewis acid silver, which is in accordance with the blue shift of the PL emission (Fig. 1(c)).

To prepare core-only AIS QDs with shorter reaction times, the ability of the MW-synthesis in a closed vessel was exploited to perform reactions above the water boiling point (Fig. S6 in the ESM). Optimum conditions, which provided the highest QY of the AIS QDs, were found for a temperature of 100 °C and relatively long reaction times (Fig. S6 in the ESM, QY of 0.24 at 50 min). However, a moderate QY of 0.19 could be achieved at 110 °C with a relatively short reaction time of 10 min (Fig. S6 in the ESM).

The temporal evolution of the optical features of the AIS QDs during ZnS shell growth is depicted in Fig. 2. Upon addition of the shell precursor, the emission peak was blue shifted. This observation is attributed to the diffusion of Zn(II) ions into the AIS lattice, yielding quaternary alloyed/doped NCs [6, 30] in addition to the formation of an inorganic surface passivation shell of ZnS around the QD core (Fig. 2(b)). Cation diffusion

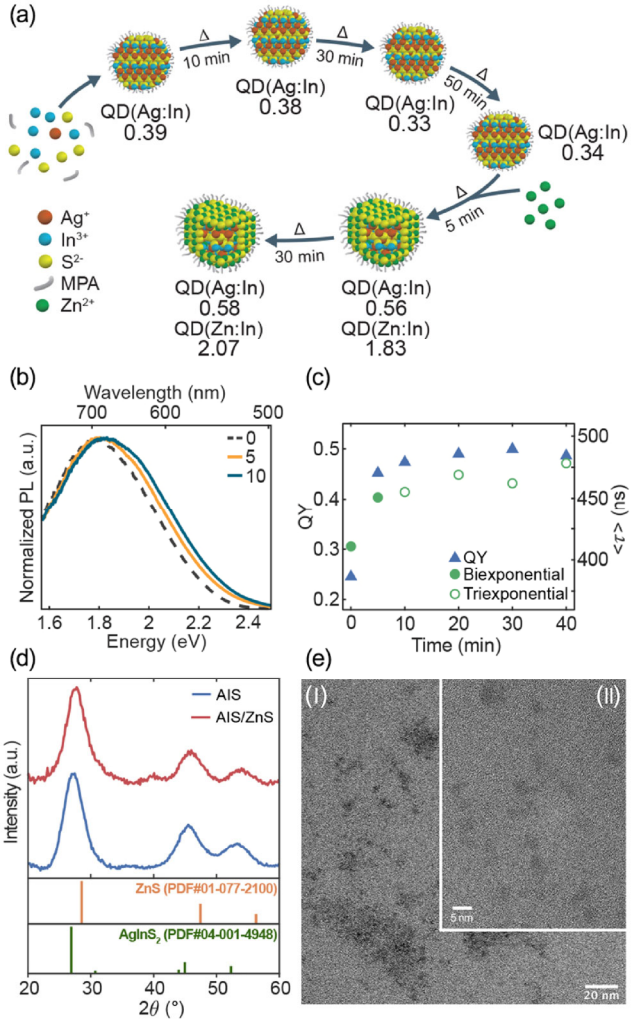

Figure 2 (a) Temporal evolution of the chemical composition of the AIS and AIS/ZnS QDs PL emission spectra. Here, QD(Ag:In) refers to the Ag:In ratio and QD(Zn:In) to the Zn:In ratio determined by ICP-OES, respectively. (b) QY and average PL lifetimes (c) of AIS QDs and AIS/ZnS QDs obtained after different reaction times. (d) XRD diffraction pattern of AIS QDs, AIS/ZnS QDs and comparison with the XRD pattern of bulk chalcopyrite $AgInS_2$ and cubic ZnS. (e) Low-magnification TEM image (I) and HR-TEM image (II) of the AIS/ZnS QDs obtained after 30 min.

into the AIS core is limited because at longer reaction time, no further blue-shift in emission was observed (data not shown). Similarly, the QY values increased considerably during the first minutes of the reaction, followed by a slow increase until a maximum value of 0.50 was reached (Fig. 2(c)). As the reaction proceeded, the PL lifetime also increased and the fluorescence decay kinetics became more complex, revealing at least triexponential decay kinetics (Fig. 2(c)). The change in the elemental composition of the AIS QDs after ZnS addition was confirmed by ICP-OES (see Fig. 2(a)). As Zn(II) is a relatively "soft" Lewis acid [3], it was expected that cation exchange occurred preferentially to yield Ag-richer NCs. The XRD diffraction pattern also support the formation of an alloy or quaternary doped QDs (Fig. 2(d)). All diffraction peaks are located between those of bulk tetragonal $AgInS_2$ and cubic ZnS, but the corresponding peaks are slightly shifted to larger angles, as is typical for the incorporation of Zn(II) ions into chalcopyrite AIS [30, 59]. The average crystal size calculated using the Scherrer equation was 2.3 nm. The HR-TEM images of the AIS/ZnS QDs show a slight increase in size to c.a. 3 nm after Zn(II) shelling (Fig. 2(e)). This subtle size increase found by HR-TEM was not congruent with the formation of complete monolayer of ZnS. Therefore, our AIS/ZnS QDs can be most likely regarded as a quaternary alloy directly at the AIS core/shell interface rather than a pure core/shell assembly.

3.3 Screening of the synthesis parameters

Subsequently, the influence of the synthesis parameters like the molar ratios of the AIS/ZnS-constituting components (Ag:In, S:In, Zn:In), the capping ligand ratio (MPA:In), and the pH were screened. The goals were to (i) evaluate the influence of each parameter on the optical properties of the resulting AIS QDs, (ii) quantify the relevance of each parameter with respect to the application-relevant features of the QDs obtained, and (iii) assess possible interferences between the parameters. To achieve these goals, a two-level multivariate DoE was performed, in which more than one parameter was studied simultaneously. The lower and upper limits of the parameters used are summarized in Table 1. For each synthesis of the 2^{5-1} fractional factorial design approach (Table S4 in the ESM), a complete optical characterization was done by measuring λ_{max} of the PL, QY, and the PL decay kinetics (Table S5 in the ESM). QY was considered the best parameter to assess the quality of the synthetized QDs. It was thus used as an outcome to construct a mathematical model, which was subsequently used for the fitting of the experimental data. More details are provided in the ESM (Table S4 in the ESM).

T-statistics were used to assess the influence of the different optimization parameters on QY. Their interferences are summarized in Fig. 3. In this figure, the *t*-value presents a measure for the absolute difference, in terms of standard deviation, between the mean and null hypothesis that the effect is zero. Therefore, the size of the *t*-value correlates with the relevance of the effect, with higher *t*-values implying a higher importance. As the chart displays the absolute values of the effects, a color code is used to represent positive and negative effects by green and blue bars, respectively. Apparently, the MPA:In ratio is the most important parameter. It has a negative effect, meaning that a decrease of the MPA:In ratio promotes an increase in QY. The MPA:In ratio, the Ag:In ratio, the interplay between the Ag:In ratio and pH (Ag:In × pH), the interplay between the MPA:In ratio and pH (MPA:In × pH), and the pH were considered in a statistically significant manner as they are above the calculated threshold line (Fig. 3, red line) of 2.23 with the currently selected terms and an alpha risk level of 0.05. The remaining terms were regarded as insignificant and subsequently neglected.

The results are in accordance with the chemistry behind the synthesis. The reactivity of In(III) is the major reaction limiting factor. Considering the aqueous medium used for the synthesis and the hardness of In(III), this cation reacts preferentially with the hydroxide ion, forming $In(OH)_3$ rather than being incorporated into the $AgInS_2$ structure [3]. In(III) can form stable complexes with MPA, and at alkaline pH, the thiol group of MPA is able to form polynuclear complexes with Indium(III) ($In[MPA]_1^{2-}$, $In[MPA]_2^{-}$, $In[MPA]_3$, and $In[MPA]_4^{+}$ species) [38, 72]. Therefore, depending on the MPA:In ratio, the $In[MPA]_x$ complex which is formed can affect the In(III) reactivity, and thus dramatically influence QY. Considering the Ag(I) and In(III) softness mismatch, the preparation of AIS/ZnS QDs requires the use of a non-stoichiometric amount of In(III). Therefore, the extent of non-stoichiometry, expressed by the Ag:In ratio, is directly related to the quality of the synthesized QDs. In the presence of cation mismatch, the pH plays a major role in the formation of alloyed QDs [3]. The pH can influence the MPA charge and then eventually on the formation of indium(III) hydroxide or zinc(II) hydroxide. Therefore, it is reasonable to assume that the interaction of the pH value with the MPA:In ratio, and the interaction of the pH with the Ag:In ratio was more significant than the pH value itself. On the other hand, the sulfide ions were present in excess compared to the amount of limiting reagent Ag(I), providing a sufficient chalcogenide pool concentration. The evidence of sulfide excess also supports the formation of a chalcopyrite $AgInS_2$-based nanostructure instead of a cubic $AgIn_5S_8$-based nanostructure. Similarly, Zn(II) was also present in excess and its diffusion into the AIS lattice rapidly reached a saturation point. Therefore, the S:In and Zn:In ratios used seemed not to be important for the QY values obtained for the AIS/ZnS QDs (Fig. 3). Contrary to the Ag:In and MPA:In ratios, the interplay between pH and S:In or Zn:In ratios were also not relevant for the QY of the AIS QDs. This suggests that the pH does not influence the HS^-/S^{2-} equilibrium nor the formation of zinc(II) hydroxide to an extent that reduces the required effective ion concentrations. As these parameters had a negative effect on QY, both were set to a value below 1 during the subsequent optimization.

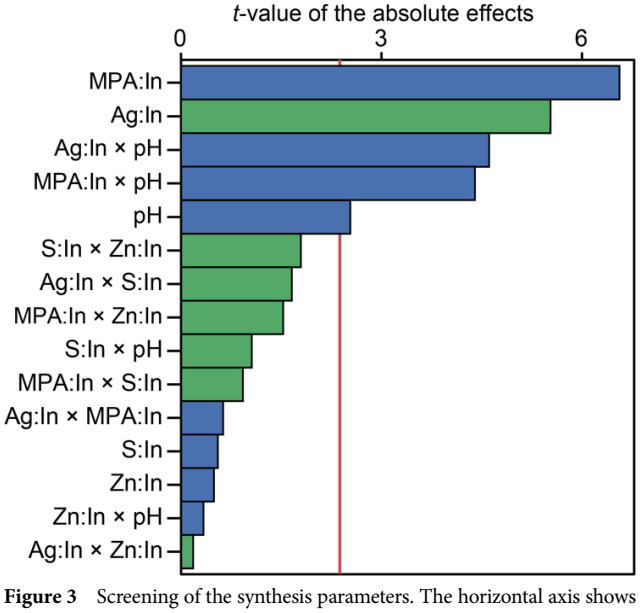

Figure 3 Screening of the synthesis parameters. The horizontal axis shows the *t*-values of the different effects assessed and the vertical axis shows each equation term. Positive effects on QY are indicated by green and negative effects by blue bars, respectively. The red line represents the threshold to be considered as significant term.

3.4 Modelling of the AIS/ZnS QDs synthesis

Once the three most important parameters were identified, they were fine-tuned by a central composite design (CCD) comprising 19 experiments. This multivariate design of experiment was chosen because it involves replicated synthesis to improve the model predictability and to estimate experimentally related errors [73, 74]. Each parameter was evaluated at five different levels and under extreme conditions [75] (Table S7 in the ESM). For one of the extreme conditions, namely performing the reaction with a MPA:In ratio of 2.6 (entry 11, Table S7 in the ESM), a white precipitate, possibly indium hydroxide, was formed during synthesis (data not shown). This indicates that a MPA:In ratio of at least 4 is required to guarantee the complete dissolution of In(III). The QD samples obtained under these conditions were thus not used for the construction of the models. The remaining 18 samples were fully characterized by steady-state (λ_{max} and QY) and time-resolved PL measurements (average lifetime, $<\tau>$) and in terms of the elemental composition of the obtained QDs (QD(Ag:In) and QD(Zn:In)) by ICP-OES (Table S8 in the ESM). For the sake of a more practical method, the PL emission maxima were expressed on a wavelength scale (λ_{max}) using the spectra directly provided by the spectrofluorometer. Based upon this large collection of experimental data, five models were predicted, one for each outcome of the reaction (Table 2).

A quadratic equation was the best fitting model for all the different sets of our experimental data (Table 2). The model equations predict the response value by substituting *a*, *b*, and *c* for the corresponding experimental parameters Ag:In ratio, MPA:In ratio, and pH. Within the range of the experimentally varied parameters used in this work, the predicted response was within the validated response range (Table 2). All models were significant with *p*-values > *F* lower than 0.0001 (ANOVA analysis). The goodness of the fits, assessed by the adjusted-R^2 and the predicted-R^2 values, was considered excellent based on the size of the obtained adjusted- and predicted-R^2 values exceeding 0.9 and 0.8, respectively [76]. Moreover, the Lack-of-Fit test, used to evaluate the goodness of the fits (in addition to R^2), yielded insignificant results (*p*-value > *F* higher than 0.05). This finding indicated that our models were valid. Adequate precision and a metric of signal-to-noise ratio indicated a suitable model discrimination (desirable > 4) [77]. More details and further analysis of the statistics behind our models are provided in the ESM (Tables S9–S13 in the ESM).

3.5 Optimization to QY

As previously stated, QY is the best parameter to assess the quality of the synthesized AIS/ZnS QDs. Therefore, based on the developed QY model, a rational design of ternary QDs was done with special emphasis on AIS/ZnS QDs with the highest QY.

The correlation between the QY values and different synthetic parameters previously identified is depicted in Fig. 4. Based on our experimental data-based QY model, highly luminescent AIS/ZnS QDs, with QY > 0.5 can be obtained by performing the synthesis at a pH between 8.5 and 9.5 (Fig. 4(a)), a MPA:In ratio between 4.5 and 6.5 (Fig. 4(a)), and an Ag:In ratio between 0.13 and 0.22 (Fig. 4(b)), respectively. The numeric resolution of the QY model focused on the highest QY values predicted for the following reaction conditions: an Ag:In ratio of 0.18, a MPA:In ratio of 5.77, and a pH of 8.91. Subsequently, five replicated syntheses were performed using these conditions in order to experimentally validate the QY model. The predicted and experimentally obtained QY values are summarized in Fig. 4(c). The excellent agreement between these values confirm the accuracy of our experimental-based model.

Our model was developed based on syntheses performed using time and temperature for the screening conditions (MW irradiation for 10 min at 110 °C plus 5 min at 100 °C). By employing optimum conditions for these parameters, like a MW irradiation for 50 min at 100 °C plus 30 min at 100 °C, AIS/ZnS QDs with QY of 0.6 were obtained. Considering that the AIS/ZnS were directly synthesized in water without a post-synthesis purification, the obtained QY values are high and it is superior to the one found on previously reported MPA-capped AIS/ZnS QDs [78]. Although AIS/ZnS QDs with a higher QY have been reported so far, these QDs were synthesized by a hot-injection method in an organic solvent [10, 79, 80]. This procedure is known to typically lead to the highest QY values, yet it is more complex and requires also ligand exchange, silanization or micellar encapsulation to render the resulting QDs water-dispersible. The experimentally determined QY data shown in Fig. 4(c) were obtained from three independent syntheses. The small standard deviations underline the excellent batch-to-batch repeatability of our MW-assisted synthesis method (see Table S14 in the ESM). The optical properties of the highly emissive MPA-capped AIS/ZnS QDs (best-AIS/ZnS QDs) are summarized in Fig. 4(d). The elemental analysis of the composition of the QY-optimized AIS/ZnS QDs gave a Ag:In ratio of 0.61 and a Zn:In ratio of 1.64 (the agreement of the experimental and predicted values is further discussed in the next chapter). Apparently, the most luminescent AIS/ZnS QDs correspond to QDs with Ag:In:Zn ratios near 1:1.5:3.

Table 2 Summary of the regression models predicted for each PL response of the central composite design (CCD)

Model equations[a]	Validated response range	Model *F*-value	Model (*p*-value > *F*)	Lack-of-fit (*p*-value > *F*)	Adjusted R^2	Predicted R^2	Adequate precision
$QY = -3.64 + 2.68a + 0.24b + 0.72c + 0.03ab + 0.04ac - 0.01bc - 9.24a^2 - 0.01b^2 - 0.04c^2$	0.205–0.524	44.31	< 0.0001	0.2375	0.9582	0.8538	19.62
$\lambda_{max} = 1144.99 + 1797.47a - 3.60b - 166.23c - 6.25ab - 157.50ac + 0.62bc - 60.98a^2 + 0.30b^2 + 11.50c^2$	617–733 nm	86.32	< 0.0001	0.2128	0.9783	0.9065	35.31
$QD(Ag:In) = -2.28 + 3.52a + 0.01b + 0.50c - 0.03ab - 0.09ac + 0.01bc + 2.11a^2 - 0.05b^2 - 0.03c^2$	0.25–1.04	538.96	< 0.0001	0.3285	0.9965	0.9865	84.39
$QD(Zn:In) = -8.71 - 8.40a + 0.20b + 2.53c - 0.07ab - 0.04ac - 0.01bc + 14.49a^2 - 0.01b^2 - 0.15c^2$	0.56–1.92	84.90	< 0.0001	0.5112	0.9780	0.9285	37.91
$<\tau> = 645.6 + 5186.3a - 14.3b - 141.8c - 3.5ab - 528.3ac - 2.8bc + 742.1a^2 + 3.7b^2 + 13.6c^2$	398–619 ns	35.43	< 0.0001	0.1444	0.9480	0.8037	21.98

[a]In the model equations *a* is the feeding Ag:In ratio used for the QD synthesis, which was validated for values between 0.1 and 0.3; *b* is the feeding MPA:In ratio, which was validated for values between 4 and 8; *c* is the pH of the reaction, which was validated for values between 8.5 and 10.5. QD(Ag:In) and QD(Zn:In) refers to the corresponding ratios present in the resulting AIS/ZnS QDs.

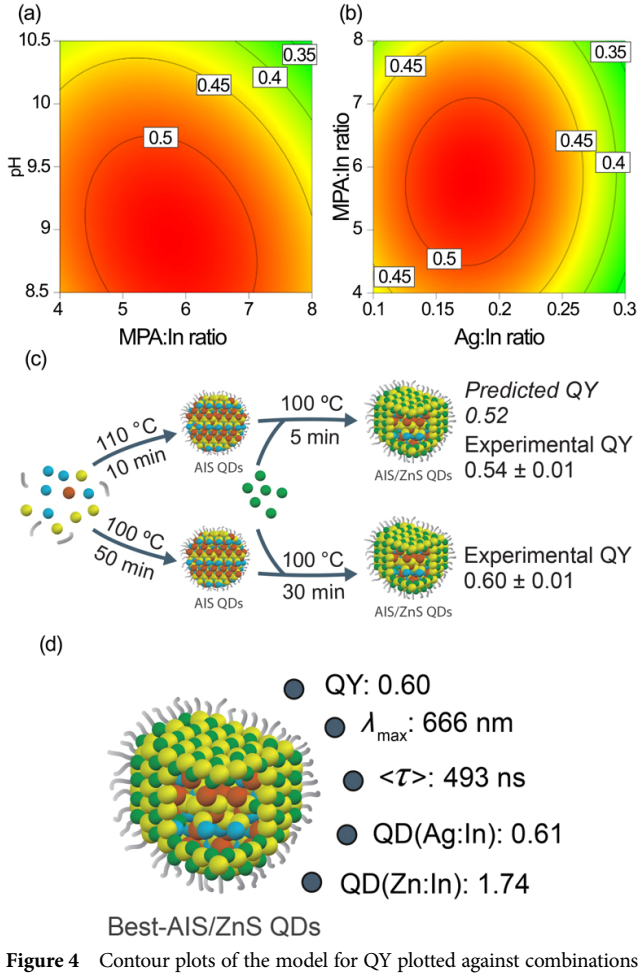

Figure 4 Contour plots of the model for QY plotted against combinations of different pH values and different MPA:In ratios (a) and combinations of different MPA:In and Ag:In ratios (b). The contour values are displayed using rounded QY values. (c) Comparison of the predicted and experimentally obtained QYs of AIS/ZnS QDs prepared with screening and optimum conditions. (d) Summary of PL properties and chemical composition of the optimum AIS/ZnS QDs, where QD(Ag:In) refers to the Ag:In ratio and QD(Zn:In) to the Zn:In ratio determined by ICP-OES, respectively.

3.6 Optimization of the tunability of PL emission

The emission of the AIS/ZnS QDs can be tuned by the feeding ratios of the precursors. However, due to the use of non-stoichiometric ratios, it is expected that the precursor ratios used in the reaction mixture can be different from the actual elemental composition of the resulting AIS/ZnS NCs. Therefore, a rational design was developed, that provides not only highly luminescent AIS/ZnS QDs, but also AIS/ZnS QDs with a defined emission wavelength and a known chemical composition. Additionally, also $<\tau>$ was considered. However, this value is not as relevant as the parameters QY and λ_{max}, and eventually also the FWHM of the PL band and additionally considering the multiexponential nature of the PL decay kinetics (and hence its challenging to fit) together with its often pronounced dependence on emission wavelength (and possibly also on excitation wavelength that was, however, beyond the scope of this study) can introduce a certain uncertainty into the derived PL lifetimes.

The correlation between the different parameters examined and the features derived from our models are shown in Fig. 5 as surface and contour plots. The surface plots were generated as a function of two parameters while the third parameter was kept constant. Visual inspection of the surface plot allows the rational design of AIS/ZnS QDs with the desired PL properties, while the exact value can be predicted by substitution of the equation parameters provided in Table 2.

Considering the target of this optimization, the tunability of the AIS/ZnS QD emission, can mainly be achieved by a low pH-focused and a low Ag(I)-focused strategy using a low value (pH of 8.5), while the Ag:In ratio is increased (Fig. 5(a), grey arrow). For the low Ag-based strategy, the Ag:In ratios maintained constant at a low value (Ag:In ratio of 8.5), while the pH is increased (Fig. 5(a), dashed arrow). The identification and use of more than one strategy to achieve the same goal emphasizes the role of DoE and its multivariate nature, as such predictions are only possible when more than one parameter is studied at the same time.

Following the low pH-focused strategy by fixing the pH at 8.5 and increasing the Ag:In ratio from 0.1 to 0.3, λ_{max} was red-shifted from about 630 to 700 nm (Fig. 5(a), grey arrow). Under these conditions, the MPA:In ratio was not that relevant for the emission tunability, as λ_{max} did not change significantly for the different MPA:In ratios used (Fig. 5(d)). In a similar manner as λ_{max}, also $<\tau>$ increased with increasing Ag:In ratio from 0.1 to 0.3 and a pH of 8.5 (Fig. 5(b)). Independent of the optimization strategy employed, a red shift is always associated with PL broadening (see Fig. S12 in the ESM). However, the large FWHM originates mainly from an intrinsic inhomogeneous PL broadening [19] with possible (smaller) contributions from the size polydispersity, distribution in composition, and Ostwald ripening. Moreover, the MPA:In ratio also did not have a significant impact on the response of $<\tau>$ (Fig. 5(e)). In terms of chemical composition, the Ag:In ratio effectively present in the AIS/ZnS QDs (QD(Ag:In) ratio) increased with increasing Ag:In ratio used in the reaction mixture (Ag:In ratio) (Fig. 5(c)), a feature frequently found on I–III–VI QDs [81], while the effective Zn:In ratio found in the AIS/ZnS QDs (QD(Zn:In) ratio) decreased slightly (Fig. 5(f)). This finding is attributed to a higher exchange rate of Zn(II) for Ag(I). The low Ag-focused strategy of keeping the Ag:In ratio constant at 0.1 and increasing the pH from 8.5 to 10.5 also led to a red shift of λ_{max} (Fig. 5(a)) and to an increase of $<\tau>$ (Fig. 5(b)). Surprisingly, the Ag:In ratio effectively present in the QDs (QD(Ag:In) ratio) did not change significantly independent of the Ag:In ratio used in the reaction mixture (Fig. 5(c)). Further details and a discussion of the surface plotting of the less significant parameters are provided in the ESM.

To evaluate the feasibility of the proposed models, an optimization strategy was designed to provide AIS/ZnS QDs with the highest possible QY and with a PL emission centered at a specific wavelength. Considering the λ_{max} range described by our model, the synthetic conditions required to yield QDs emitting at 620 (QD-620), at 660 (QD-660), and at 700 nm (QD-705) were predicted. The accordingly identified synthetic conditions were (i) QD-620: Ag:In of 0.10, MPA:In of 4.42, and pH of 8.56; (ii) QD-660: Ag:In of 0.22, MPA:In of 6.22, and pH of 8.61; (iii) QD-705: Ag:In of 0.30, MPA:In of 6.59, and pH of 8.50. The predicted and experimentally determined values for QD-620, QD-660, QD-705, and QY-optimized QDs are shown in Fig. 6. The experimentally obtained PL features, here λ_{max}, were in accordance with the predicted values, as all experimental values were within the limits of the prediction interval (Fig. 6). This confirms that the models can forecast the actual outcome of different synthesis conditions. Nevertheless, the accuracy of the prediction depended on the synthesis conditions and on the model, with models with lower predicted-R^2 value revealing the expected large discrepancy between predicted and experimental outcome. As the models were based on

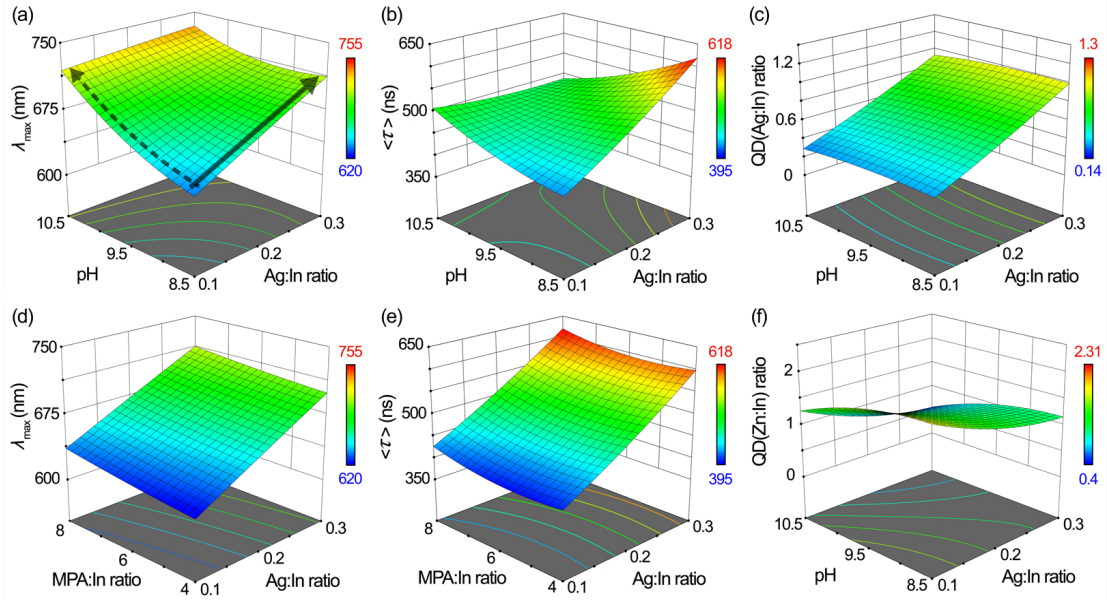

Figure 5 Surface and contour plots of the response functions of the PL features to changes in the different parameters affecting AIS/ZnS QD performance. The relation between pH, Ag:In, and λ_{max} (a), $<\tau>$ (b), QD(Ag:In) (c), and QD(Zn:In) (f), when MPA:In is fixed at 8. The relation between MPA:In, Ag:In, and λ_{max} (d), and $<\tau>$ (e), when pH is fixed at 8.5.

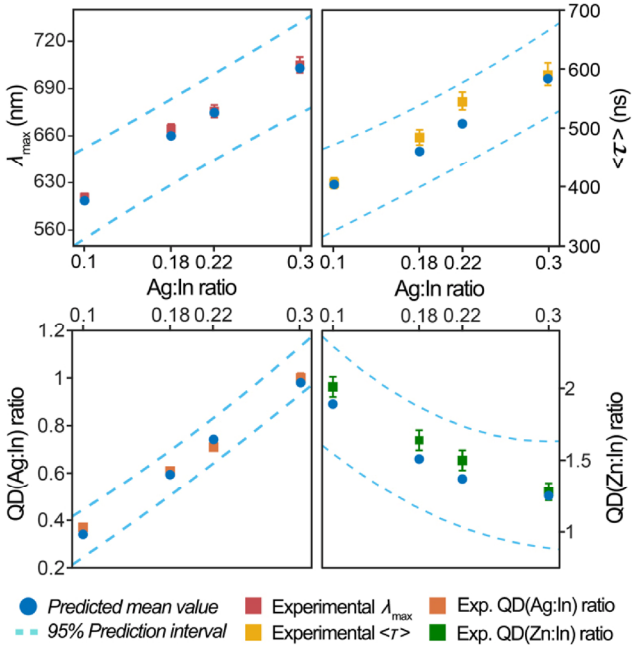

Figure 6 Comparison between the predicted and experimentally determined PL features of AIS/ZnS QDs designed with a target PL emission wavelength. The 95% prediction interval represents the interval in which 99% of the QD population lay with a 95% confidence.

experimental data, the variability in the experimental data like the relative standard deviations found for QY, PL decay measurements or the determination of the zinc(II) amount by ICP-OES were automatically reflected by the model's accuracy of predicting certain properties or reaction conditions to realize certain features. Although the prediction accuracy for most of the desired PL features can be still refined, our goal to describe the highly complex correlation between the different synthetic parameters and the optical properties for ternary core/shell QDs consisting of four different constituents and an organic ligand shell was achieved.

The range of emission wavelengths obtained with our λ_{max} model was also affected by the choice of the synthesis parameters and their allowed range in variation used for developing this experiment-based model, namely the range of considered variations in the Ag:In ratio (from 0.1 to 0.3). Utilizing the low-pH strategy, we expanded our λ_{max} model by exploring different combinations of pH and Ag:In ratios (Table S15 in the ESM). Figure 7(b) shows the PL emission spectra of AIS/ZnS QDs obtained with Ag:In ratios varying from 0.01 to 0.325. This led to QDs with λ_{max} changing from 565 to 725 nm for Ag:In of 0.01 and 0.325. A blue emission (λ_{max} < 500 nm) could not be realized, as the AIS/ZnS QDs synthesized with a very low amount of silver(I) showed only a very weak luminescence (QY of 0.05 for QDs with Ag:In of 0.01, Table S15 in the ESM). High QYs in the red region of the visible spectrum and the near infrared region were satisfactorily achieved (QY of 0.24

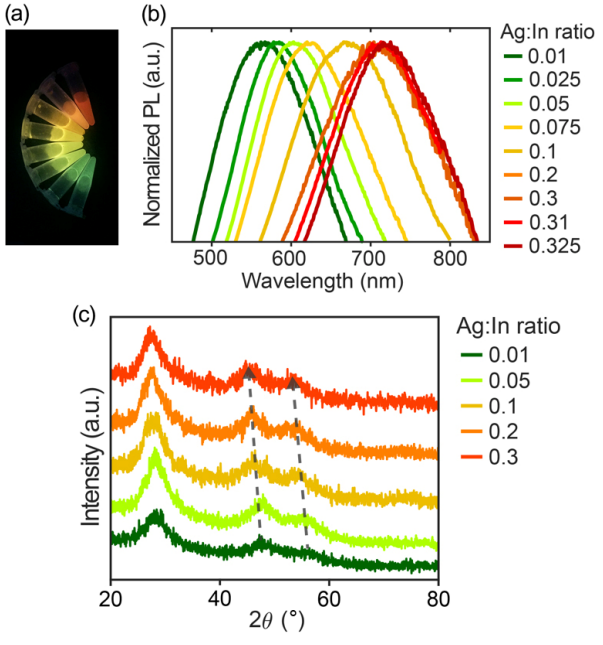

Figure 7 (a) AIS/ZnS QDs excited with a UV lamp. (b) PL emission of AIS/ZnS QDs synthetized with different Ag:In ratios; the Ag:In ratios are given in the legend. (c) XRD diffraction pattern of AIS/ZnS QDs synthetized with different Ag:In ratios.

for QDs with Ag:In of 0.325, see Table S15 in the ESM). As expected, extrapolating outside of the design space increased the prediction uncertainty because of the lack of experimental data collected for such PL properties and used for developing a model (Fig. S14 in the ESM). When the reaction is performed at low pH with increasing Ag:In feeding ratio, the Ag:In ratio present in the QDs is increased (Figs. 5(c) and 5(f)). This stoichiometric elemental composition was also reflected by the XRD pattern of the resulting QDs, as AIS/ZnS QDs synthetized with increasing Ag:In feeding ratios showed diffraction peaks of increasing sharpness shifted to smaller angles (Fig. 7(c)).

3.7 Relationship between QDs structure and PL properties

The developed models also allow to establish the relationship between the synthesis experimental conditions, the obtained AIS QDs chemical structure, and the resulting PL properties. Figure 8 summarizes three paradigmatic examples of this relationship. In the first example, AIS QDs synthesis were designed using the lowest Ag:In ratio and pH of our experimental settings (Ag:In = 0.1, pH = 8.5). These conditions yield AIS/ZnS QDs with non-stoichiometric Ag:In:Zn ratios of about 1:3:4, which emit around 620 nm, with relatively short PL lifetimes, considering the range of decays typically found for AIS/ZnS QDs (Fig. 8). A synthesis design where the Ag feeding ratio is kept low and the pH is increased (Ag:In = 0.1, pH = 10.5), leads to QDs with almost similar Ag:In:Zn ratios, while increasing the feeding Ag content at a pH of 8.5 (Ag:In = 0.3, pH = 8.5) results in almost stoichiometric AIS QD structures with Ag:In:Zn ratios of about 1:1:1 (Fig. 8). Apparently, the silver amount used in the QD synthesis is the limiting reactant for the incorporation of Ag(I) into the AIS nanocrystals, independently of the pH used for the synthesis. However, the different chemical compositions of the AIS/ZnS QDs obtained show almost the same PL emission. This effect might possibly arise from the underlying PL emission mechanism of these ternary QDs. For this complex system, it seems reasonable to assume that, depending on the synthesis conditions used, different PL mechanisms can assume a predominant role. For example, the PL red shift achieved with stoichiometric AIS/ZnS QDs could be possibly ascribed to a change in the defect sites within the QD volume. This is also reflected by changes in the PL lifetimes found in this series with values of $<\tau>$ of about 600 ns vs. 500 ns. For QDs synthetized with the conditions of pH = 8.5/Ag:In = 0.3 and pH = 10.5/Ag:In = 0.1, these effects are more pronounced than for AIS QDs with a non-stoichiometric Ag:In:Zn ratio of 1:3:4. Considering its complex and heterogeneous lattice and the lack of defined PL mechanism, the establishment of a well-defined relationship is dauting, and further research is required to better understand how these properties are interlinked.

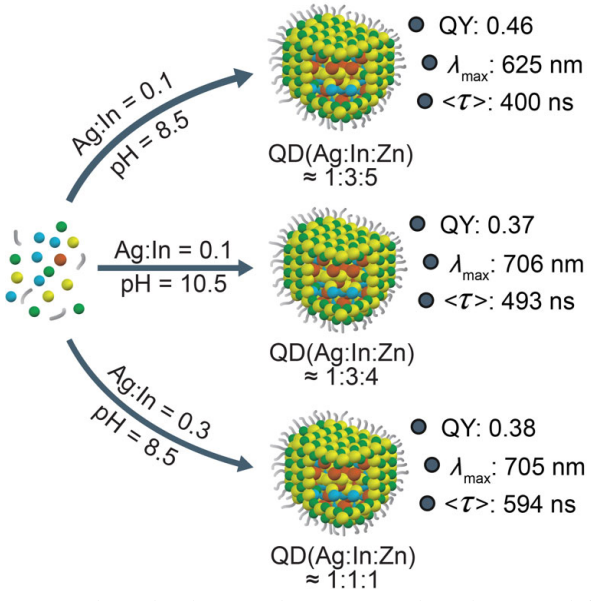

Figure 8 Relationship between the experimental conditions used for, AIS/ZnS QD synthesis and their PL properties; the MPA:In ratio was set to 6 for all the designed QDs. QD(Ag:In:Zn) refers to the Ag:In:Zn ratio effectively found in the prepared QDs.

4 Conclusions

To fulfil the high expectations imposed on cadmium-free ternary I–III–VI semiconductor QDs, a rational approach to their preparation with respect to the targeted PL features like PL emission color, spectral linewidth, QY, and for some applications involving lifetime encoding and time-gated emission, even PL decay kinetics/PL lifetime, is needed. Although ternary core–shell QDs like AIS/ZnS QDs can be obtained in high quality by a facile synthetic route in water, the proper choice of the many experimental parameters affecting the optical properties of the resulting QDs like pH, ratios of the different Ag(I), In(III), Zn(II), and sulfide precursors, temperature, and reaction time, that are often also connected, needs to be facilitated. Here, experimentally-based models for a highly reproducible and environmentally friendly microwave (MW)-assisted procedure were developed that directly correlate target PL features with synthesis parameters. This approach validated by us for different sets of AIS QDs, allows chemists to rationally design AIS/ZnS QDs with a widely tunable PL emission and with forecasted QY, as well as average PL lifetimes and elemental composition. Considering the most important features for designing bright AIS/ZnS QDs, our models revealed that QY can be steadily increased by refining the reactions conditions. Emission tunability, also with consequences in terms of PL lifetime and QD elemental composition, can be achieved either by a low pH-focused or low Ag-focused approach. Moreover, the large set of data collected in this work confirms features already described for AIS/ZnS QDs in the literature. This includes the role played by the QDs chemical composition and the proposed PL mechanisms accounting for the broad PL emission band.

In summary, we could successfully model the highly complex correlation between the different synthetic parameters and the optical properties for ternary core/shell QDs. These developments in the predictive and experiment-based modelling of the synthesis of more complex QDs, like ternary QDs containing three different metal ions with varying reactivities and a shelling step, are expected to pave the road to a deeper understanding of fundamental properties of this class of semiconductors. In the future, we plan to refine these models to further improve their prediction accuracy and to apply them also to other ternary QDs, like core and core–shell Cu–In–S (CIS) and Hg–In–S (HIS) QDs.

Acknowledgements

The authors acknowledge fruitful discussions with Irina V. Martynenko and Lorena Dhamo from division Biophotonics. The authors thank André Gardei from the division 7.1 Building Materials (BAM) for the XRD measurements. The TEM images were carried out as part of the DFG core facility project "Berlin Electron Microscopy Network (Berlin EM Network)". This work received financial support from the European Union

(FEDER funds POCI/01/0145/FEDER/007265) and National Funds (FCT/MEC, Fundação para a Ciência e Tecnologia and Ministério da Educação e Ciência) under the Partnership Agreement PT2020 UID/QUI/50006/2013 and through the FCT PhD Programmes and by Programa Operacional Potencial Humano (POCH), specifically by the BiotechHealth Programme (Doctoral Programme on Cellular and Molecular Biotechnology Applied to Health Sciences), reference PD/00016/2012. J. X. S. thanks FCT and POPH for his PhD grant (SFRH/BD/98105/2013). K. D. W. acknowledges the European Union's Horizon 2020 research and innovation programme under the Marie Sklodowska-Curie grant agreement No. 846764. URG gratefully acknowledges financial support by the German Research Council (DFG; grant RE1203/12-3).

Funding note: Open access funding provided by Projekt DEAL.

Electronic Supplementary Material: Supplementary material (preliminary assays for the synthesis of AIS/ZnS QDs, steady-state and lifetime PL measurements of AIS/ZnS QDs, elemental analysis by ICP-OES, high-resolution TEM images analysis; and detailed analysis of the statistics behind our models) is available in the online version of this article at https://doi.org/10.1007/s12274-020-2876-8.

References

[1] Aldakov, D.; Lefrancois, A.; Reiss, P. Ternary and quaternary metal chalcogenide nanocrystals: Synthesis, properties and applications. *J. Mater. Chem. C* **2013**, *1*, 3756–3776.

[2] Xu, G. X.; Zeng, S. W.; Zhang, B. T.; Swihart, M. T.; Yong, K. T.; Prasad, P. N. New generation cadmium-free quantum dots for biophotonics and nanomedicine. *Chem. Rev.* **2016**, *116*, 12234–12327.

[3] Jing, L. H.; Kershaw, S. V.; Li, Y. L.; Huang, X. D.; Li, Y. Y.; Rogach, A. L.; Gao, M. Y. Aqueous based semiconductor nanocrystals. *Chem. Rev.* **2016**, *116*, 10623–10730.

[4] Tamang, S.; Lincheneau, C.; Hermans, Y.; Jeong, S.; Reiss, P. Chemistry of InP nanocrystal syntheses. *Chem. Mater.* **2016**, *28*, 2491–2506.

[5] Li, Y.; Pu, C. D.; Peng, X. G. Surface activation of colloidal indium phosphide nanocrystals. *Nano Res.* **2017**, *10*, 941–958.

[6] Kolny-Olesiak, J.; Weller, H. Synthesis and application of colloidal $CuInS_2$ semiconductor nanocrystals. *ACS Appl. Mater. Interfaces* **2013**, *5*, 12221–12237.

[7] Li, X.; Tu, D. T.; Yu, S. H.; Song, X. R.; Lian, W.; Wei, J. J.; Shang, X. Y.; Li, R. F.; Chen, X. Y. Highly efficient luminescent I-III-VI semiconductor nanoprobes based on template-synthesized $CuInS_2$ nanocrystals. *Nano Res.* **2019**, *12*, 1804–1809.

[8] Nakamura, H.; Kato, W.; Uehara, M.; Nose, K.; Omata, T.; Otsuka-Yao-Matsuo, S.; Miyazaki, M.; Maeda, H. Tunable photoluminescence wavelength of chalcopyrite $CuInS_2$-based semiconductor nanocrystals synthesized in a colloidal system. *Chem. Mater.* **2006**, *18*, 3330–3335.

[9] Xia, C. H.; Meeldijk, J. D.; Gerritsen, H. C.; Donega, C. d. M. Highly luminescent water-dispersible nir-emitting wurtzite $CuInS_2$/ZnS core/shell colloidal quantum dots. *Chem. Mater.* **2017**, *29*, 4940–4951.

[10] Ko, M.; Yoon, H. C.; Yoo, H.; Oh, J. H.; Yang, H.; Do, Y. R. Highly efficient green Zn-Ag-In-S/Zn-In-S/ZnS QDs by a strong exothermic reaction for down-converted green and tripackage white LEDs. *Adv. Funct. Mater.* **2017**, *27*, 1602638.

[11] Raevskaya, A.; Lesnyak, V.; Haubold, D.; Dzhagan, V.; Stroyuk, O.; Gaponik, N.; Zahn, D. R. T.; Eychmüller, A. A fine size selection of brightly luminescent water-soluble Ag–In–S and Ag–In–S/ZnS quantum dots. *J. Phys. Chem. C* **2017**, *121*, 9032–9042.

[12] van der Stam, W.; Berends, A. C.; Rabouw, F. T.; Willhammar, T.; Ke, X. X.; Meeldijk, J. D.; Bals, S.; Donega, C. d. M. Luminescent $CuInS_2$ quantum dots by partial cation exchange in $Cu_{2-x}S$ nanocrystals. *Chem. Mater.* **2015**, *27*, 621–628.

[13] Han, N. S.; Yoon, H. C.; Jeong, S.; Oh, J. H.; Park, S. M.; Do, Y. R.; Song, J. K. Origin of highly efficient photoluminescence in $AgIn_5S_8$ nanoparticles. *Nanoscale* **2017**, *9*, 10285–10291.

[14] Stroyuk, O.; Weigert, F.; Raevskaya, A.; Spranger, F.; Würth, C.; Resch-Genger, U.; Gaponik, N.; Zahn, D. R. T. Inherently broadband photoluminescence in Ag–In–S/ZnS quantum dots observed in ensemble and single-particle studies. *J. Phys. Chem. C* **2019**, *123*, 2632–2641.

[15] Dai, M. L.; Ogawa, S.; Kameyama, T.; Okazaki, K. I.; Kudo, A.; Kuwabata, S.; Tsuboi, Y.; Torimoto, T. Tunable photoluminescence from the visible to near-infrared wavelength region of non-stoichiometric $AgInS_2$ nanoparticles. *J. Mater. Chem.* **2012**, *22*, 12851–12858.

[16] Tsuji, I.; Kato, H.; Kobayashi, H.; Kudo, A. Photocatalytic H_2 evolution reaction from aqueous solutions over band structure-controlled $(AgIn)_xZn_{2(1-x)}S_2$ solid solution photocatalysts with visible-light response and their surface nanostructures. *J. Am. Chem. Soc.* **2004**, *126*, 13406–13413.

[17] Stroyuk, O.; Raevskaya, A.; Spranger, F.; Selyshchev, O.; Dzhagan, V.; Schulze, S.; Zahn, D. R. T.; Eychmüller, A. Origin and dynamics of highly efficient broadband photoluminescence of aqueous glutathione-capped size-selected Ag-In-S quantum dots. *J. Phys. Chem. C* **2018**, *122*, 13648–13658.

[18] Zang, H. D.; Li, H. B.; Makarov, N. S.; Velizhanin, K. A.; Wu, K. F.; Park, Y. S.; Klimov, V. I. Thick-shell $CuInS_2$/ZnS quantum dots with suppressed "blinking" and narrow single-particle emission line widths. *Nano Lett.* **2017**, *17*, 1787–1795.

[19] Martynenko, I. V.; Baimuratov, A. S.; Weigert, F.; Soares, J. X.; Dhamo, L.; Nickl, P.; Doerfel, I.; Pauli, J.; Rukhlenko, I. D.; Baranov, A. V. et al. Photoluminescence of Ag-In-S/ZnS quantum dots: Excitation energy dependence and low-energy electronic structure. *Nano Res.* **2019**, *12*, 1595–1603.

[20] Peng, L. C.; Li, D. Z.; Zhang, Z. L.; Huang, K. K.; Zhang, Y.; Shi, Z.; Xie, R. G.; Yang, W. S. Large-scale synthesis of single-source, thermally stable, and dual-emissive Mn-doped Zn-Cu-In-S nanocrystals for bright white light-emitting diodes. *Nano Res.* **2015**, *8*, 3316–3331.

[21] Jara, D. H.; Yoon, S. J.; Stamplecoskie, K. G.; Kamat, P. V. Size-dependent photovoltaic performance of $CuInS_2$ quantum dot-sensitized solar cells. *Chem. Mater.* **2014**, *26*, 7221–7228.

[22] Stroyuk, O.; Raevskaya, A.; Gaponik, N. Solar light harvesting with multinary metal chalcogenide nanocrystals. *Chem. Soc. Rev.* **2018**, *47*, 5354–5422.

[23] Regulacio, M. D.; Han, M. Y. Multinary I-III-VI_2 and I_2-II-IV-VI_4 semiconductor nanostructures for photocatalytic applications. *Acc. Chem. Res.* **2016**, *49*, 511–519.

[24] Liu, X. Y.; Zhang, G. Z.; Chen, H.; Li, H. W.; Jiang, J.; Long, Y. T.; Ning, Z. J. Efficient defect-controlled photocatalytic hydrogen generation based on near-infrared Cu-In-Zn-S quantum dots. *Nano Res.* **2018**, *11*, 1379–1388.

[25] Li, L.; Daou, T. J.; Texier, I.; Chi, T. H. K.; Liem, N. Q.; Reiss, P. Highly luminescent $CuInS_2$/ZnS core/shell nanocrystals: Cadmium-free quantum dots for *in vivo* imaging. *Chem. Mater.* **2009**, *21*, 2422–2429.

[26] Deng, D. W.; Chen, Y. Q.; Cao, J.; Tian, J. M.; Qian, Z. Y.; Achilefu, S.; Gu, Y. Q. High-quality $CuInS_2$/ZnS quantum dots for *in vitro* and *in vivo* bioimaging. *Chem. Mater.* **2012**, *24*, 3029–3037.

[27] Ogihara, Y.; Yukawa, H.; Kameyama, T.; Nishi, H.; Onoshima, D.; Ishikawa, T.; Torimoto, T.; Baba, Y. Labeling and *in vivo* visualization of transplanted adipose tissue-derived stem cells with safe cadmium-free aqueous ZnS coating of ZnS-$AgInS_2$ nanoparticles. *Sci. Rep.* **2017**, *7*, 40047.

[28] Du, W. M.; Qian, X. F.; Yin, J.; Gong, Q. Shape- and phase-controlled synthesis of monodisperse, single-crystalline ternary chalcogenide colloids through a convenient solution synthesis strategy. *Chem. –Eur. J.* **2007**, *13*, 8840–8846.

[29] Berends, A. C.; Mangnus, M. J. J.; Xia, C. H.; Rabouw, F. T.; Donega, C. d. M. Optoelectronic properties of ternary I–III–VI_2 semiconductor nanocrystals: Bright prospects with elusive origins. *J. Phys. Chem. Lett.* **2019**, *10*, 1600–1616.

[30] Regulacio, M. D.; Win, K. Y.; Lo, S. L.; Zhang, S. Y.; Zhang, X. H.; Wang, S.; Han, M. Y.; Zheng, Y. G. Aqueous synthesis of highly luminescent $AgInS_2$-ZnS quantum dots and their biological applications. *Nanoscale* **2013**, *5*, 2322–2327.

[31] Luo, Z. S.; Zhang, H.; Huang, J.; Zhong, X. H. One-step synthesis of water-soluble $AgInS_2$ and ZnS-$AgInS_2$ composite nanocrystals and their photocatalytic activities. *J. Colloid Interface Sci.* **2012**, *377*, 27–33.

[32] Song, J. L. Q.; Ma, C.; Zhang, W. Z.; Li, X. D.; Zhang, W. T.; Wu, R. B.; Cheng, X. C.; Ali, A.; Yang, M. Y.; Zhu, L. X. et al. Bandgap and structure engineering via cation exchange: From binary Ag_2S to ternary $AgInS_2$, quaternary AgZnInS alloy and AgZnInS/ZnS core/shell fluorescent nanocrystals for bioimaging. *ACS Appl. Mater. Interfaces* **2016**, *8*, 24826–24836.

[33] Doh, H.; Hwang, S.; Kim, S. Size-tunable synthesis of nearly monodisperse Ag_2S nanoparticles and size-dependent fate of the crystal structures upon cation exchange to $AgInS_2$ nanoparticles. *Chem. Mater.* **2016**, *28*, 8123–8127.

[34] Mao, B. D.; Chuang, C. H.; Lu, F.; Sang, L. X.; Zhu, J. J.; Burda, C. Study of the partial Ag-to-Zn cation exchange in $AgInS_2$/ZnS nanocrystals. *J. Phys. Chem. C* **2013**, *117*, 648–656.

[35] Berends, A. C.; van der Stam, W.; Hofmann, J. P.; Bladt, E.; Meeldijk, J. D.; Bals, S.; Donega, C. d. M. Interplay between surface chemistry, precursor reactivity, and temperature determines outcome of ZnS shelling reactions on $CuInS_2$ nanocrystals. *Chem. Mater.* **2018**, *30*, 2400–2413.

[36] Fernando, Q.; Freiser, H. Chelating properties of β-mercaptopropionic acid. *J. Am. Chem. Soc.* **1958**, *80*, 4928–4931.

[37] Sarin, R.; Munshi, K. N. Physico-chemical investigation on the complexes of indium(III) with mercapto-, hydroxy-, and amino-substituted propionic acid. *Aust. J. Chem.* **1972**, *25*, 929–939.

[38] Kojima, N.; Sugiura, Y.; Tanaka, H. Polynuclear and mononuclear complex formation between indium (III) and sulfhydryl-containing bidentate ligands. *Chem. Pharm. Bull.* **1978**, *26*, 579–584.

[39] He, Y.; Sai, L.M.; Lu, H. T.; Hu, M.; Lai, W. Y.; Fan, Q. L.; Wang, L. H.; Huang, W. Microwave-assisted synthesis of water-dispersed CdTe nanocrystals with high luminescent efficiency and narrow size distribution. *Chem. Mater.* **2007**, *19*, 359–365.

[40] Duan, J. L.; Song, L. X.; Zhan, J. H. One-pot synthesis of highly luminescent CdTe quantum dots by microwave irradiation reduction and their Hg^{2+}-sensitive properties. *Nano Res.* **2009**, *2*, 61–68.

[41] Hayakawa, Y.; Nonoguchi, Y.; Wu, H. P.; Diau, E. W. G.; Nakashima, T.; Kawai, T. Rapid preparation of highly luminescent CdTe nanocrystals in an ionic liquid via a microwave-assisted process. *J. Mater. Chem.* **2011**, *21*, 8849–8853.

[42] He, Y.; Lu, H. T.; Sai, L. M.; Lai, W. Y.; Fan, Q. L.; Wang, L. H.; Huang, W. Synthesis of CdTe nanocrystals through program process of microwave irradiation. *J. Phys. Chem. B* **2006**, *110*, 13352–13356.

[43] Li, L.; Qian, H. F.; Ren, J. C. Rapid synthesis of highly luminescent CdTe nanocrystals in the aqueous phase by microwave irradiation with controllable temperature. *Chem. Commun.* **2005**, *36*, 528–530.

[44] Mousavi-Kamazani, M.; Salavati-Niasari, M. A simple microwave approach for synthesis and characterization of Ag_2S-$AgInS_2$ nano-composites. *Compos. Part B Eng.* **2014**, *56*, 490–496.

[45] Tadjarodi, A.; Cheshmekhavar, A. H.; Imani, M. Preparation of $AgInS_2$ nanoparticles by a facile microwave heating technique; Study of effective parameters, optical and photovoltaic characteristics. *Appl. Surf. Sci.* **2012**, *263*, 449–456.

[46] Xiong, W. W.; Yang, G. H.; Wu, X. C.; Zhu, J. J. Microwave-assisted synthesis of highly luminescent $AgInS_2$/ZnS nanocrystals for dynamic intracellular Cu(II) detection. *J. Mater. Chem. B* **2013**, *1*, 4160–4165.

[47] Zhang, W. J.; Li, D. Z.; Chen, Z. X.; Sun, M.; Li, W. J.; Lin, Q.; Fu, X. Z. Microwave hydrothermal synthesis of $AgInS_2$ with visible light photocatalytic activity. *Mater. Res. Bull.* **2011**, *46*, 975–982.

[48] Mir, I. A.; Radhakrishanan, V. S.; Rawat, K.; Prasad, T.; Bohidar, H. B. Bandgap tunable AgInS based quantum dots for high contrast cell imaging with enhanced photodynamic and antifungal applications. *Sci. Rep.* **2018**, *8*, 9322.

[49] Raveendran, S.; Sen, A.; Maekawa, T.; Kumar, D. S. Ultra-fast microwave aided synthesis of gold nanocages and structural maneuver studies. *Nano Res.* **2017**, *10*, 1078–1091.

[50] Zhang, J.; Yuan, Y.; Wang, Y.; Sun, F. F.; Liang, G. L.; Jiang, Z.; Yu, S. H. Microwave-assisted synthesis of photoluminescent glutathione-capped Au/Ag nanoclusters: A unique sensor-on-a-nanoparticle for metal ions, anions, and small molecules. *Nano Res.* **2015**, *8*, 2329–2339.

[51] Horikoshi, S.; Serpone, N. Considerations of microwave heating. In *Microwaves in Nanoparticle Synthesis*: *Fundamentals and Applications*. Horikoshi, S., Serpone, N., Eds.; Wiley: Weinheim, 2013; pp 39–54.

[52] Denmark, S. E.; Butler, C. R. Vinylation of aromatic halides using inexpensive organosilicon reagents. Illustration of design of experiment protocols. *J. Am. Chem. Soc.* **2008**, *130*, 3690–3704.

[53] Ribeiro, D. S. M.; de Souza, G. C. S.; Melo, A.; Soares, J. X.; Rodrigues, S. S. M.; Araújo, A. N.; Montenegro, M. C. B. S. M.; Santos, J. L. M. Synthesis of distinctly thiol-capped CdTe quantum dots under microwave heating: Multivariate optimization and characterization. *J. Mater. Sci.* **2017**, *52*, 3208–3224.

[54] Braham, E. J.; Cho, J.; Forlano, K. M.; Watson, D. F.; Arròyave, R.; Banerjee, S. Machine learning-directed navigation of synthetic design space: A statistical learning approach to controlling the synthesis of perovskite halide nanoplatelets in the quantum-confined regime. *Chem. Mater.* **2019**, *31*, 3281–3292.

[55] Song, J. H.; Xie, H. Z.; Wu, W. Z.; Joseph, V. R.; Wu, C. F. J.; Wang, Z. L. Robust optimization of the output voltage of nanogenerators by statistical design of experiments. *Nano Res.* **2010**, *3*, 613–619.

[56] Protière, M.; Nerambourg, N.; Renard, O.; Reiss, P. Rational design of the gram-scale synthesis of nearly monodisperse semiconductor nanocrystals. *Nanoscale Res. Lett.* **2011**, *6*, 472.

[57] Hoffmann, K.; Behnke, T.; Drescher, D.; Kneipp, J.; Resch-Genger, U. Near-infrared-emitting nanoparticles for lifetime-based multiplexed analysis and imaging of living cells. *Acs Nano* **2013**, *7*, 6674–6684.

[58] Liu, S. Y.; Zhang, H.; Qiao, Y.; Su, X. G. One-pot synthesis of ternary $CuInS_2$ quantum dots with near-infrared fluorescence in aqueous solution. *RSC Adv.* **2012**, *2*, 819–825.

[59] Deng, D. W.; Qu, L. Z.; Cheng, Z. Q.; Achilefu, S.; Gu, Y. Q. Highly luminescent water-soluble quaternary Zn-Ag-In-S quantum dots and their unique precursor S/In ratio-dependent spectral shifts. *J. Lumin.* **2014**, *146*, 364–370.

[60] Xie, R. G.; Rutherford, M.; Peng, X. G. Formation of high-quality I−III−VI semiconductor nanocrystals by tuning relative reactivity of cationic precursors. *J. Am. Chem. Soc.* **2009**, *131*, 5691–5697.

[61] Kadlag, K. P.; Patil, P.; Rao, M. J.; Datta, S.; Nag, A. Luminescence and solar cell from ligand-free colloidal $AgInS_2$ nanocrystals. *Crystengcomm* **2014**, *16*, 3605–3612.

[62] Cichy, B.; Olejniczak, A.; Bezkrovnyi, O.; Kepinski, L.; Strek, W. Defects mediated charge disturbance in quantum-confined Ag_xS/$AgIn_{S2}$ random alloys—Toward slowly decaying quantum dot emitters. *J. Alloys Compd.* **2019**, *798*, 290–299.

[63] Yang, J.; Muckel, F.; Baek, W.; Fainblat, R.; Chang, H.; Bacher, G.; Hyeon, T. Chemical synthesis, doping, and transformation of magic-sized semiconductor alloy nanoclusters. *J. Am. Chem. Soc.* **2017**, *139*, 6761–6770.

[64] Bajwa, P.; Gao, F.; Nguyen, A.; Omogo, B.; Heyes, C. D. Influence of the inner-shell architecture on quantum yield and blinking dynamics in core/multishell quantum dots. *Chemphyschem* **2016**, *17*, 731–740.

[65] Chen, O.; Zhao, J.; Chauhan, V. P.; Cui, J.; Wong, C.; Harris, D. K.; Wei, H.; Han, H. S.; Fukumura, D.; Jain, R. K. et al. Compact high-quality CdSe–CdS core–shell nanocrystals with narrow emission linewidths and suppressed blinking. *Nat. Mater.* **2013**, *12*, 445–451.

[66] Greytak, A. B.; Allen, P. M.; Liu, W. H.; Zhao, J.; Young, E. R.; Popović, Z.; Walker, B. J.; Nocera, D. G.; Bawendi, M. G. Alternating layer addition approach to CdSe/CdS core/shell quantum dots with near-unity quantum yield and high on-time fractions. *Chem. Sci.* **2012**, *3*, 2028–2034.

[67] Vela, J.; Htoon, H.; Chen, Y. F.; Park, Y. S.; Ghosh, Y.; Goodwin, P. M.; Werner, J. H.; Wells, N. P.; Casson, J. L.; Hollingsworth, J. A. Effect of shell thickness and composition on blinking suppression and the blinking mechanism in "giant" CdSe/CdS nanocrystal quantum dots. *J. Biophotonics* **2010**, *3*, 706–717.

[68] van der Stam, W.; Berends, A. C.; Donega, C. d. M. Prospects of colloidal copper chalcogenide nanocrystals. *Chemphyschem* **2016**, *17*, 559–581.

[69] Donega, C. d. M.; Koole, R. Size dependence of the spontaneous emission rate and absorption cross section of CdSe and CdTe quantum dots. *J. Phys. Chem. C* **2009**, *113*, 6511–6520.

[70] Fisher, B. R.; Eisler, H. J.; Stott, N. E.; Bawendi, M. G. Emission intensity dependence and single-exponential behavior in single colloidal quantum dot fluorescence lifetimes. *J. Phys. Chem. B* **2004**, *108*, 143–148.

[71] van Driel, A. F.; Allan, G.; Delerue, C.; Lodahl, P.; Vos, W. L.; Vanmaekelbergh, D. Frequency-dependent spontaneous emission rate from CdSe and CdTe nanocrystals: Influence of dark states. *Phys. Rev. Lett.* **2005**, *95*, 236804.

[72] Sarin, R.; Munshi, K. N. Stability constants and thermodynamic functions of indium(III) complexes with some organic acids from potentiometric data. *J. Inorg. Nucl. Chem.* **1973**, *35*, 201–207.

[73] Tarley, C. R. T.; Silveira, G.; dos Santos, W. N. L.; Matos, G. D.; da Silva, E. G. P.; Bezerra, M. A.; Miró, M.; Ferreira, S. L. C. Chemometric tools in electroanalytical chemistry: Methods for optimization based on factorial design and response surface methodology. *Microchem. J.* **2009**, *92*, 58–67.

[74] Keskin Gündoğdu, T.; Deniz, İ.; Çalışkan, G.; Şahin, E. S.; Azbar, N. Experimental design methods for bioengineering applications. *Crit. Rev. Biotechnol.* **2016**, *36*, 368–388.

[75] Khuri, A. I.; Mukhopadhyay, S. Response surface methodology. *Wiley Interdiscip. Rev. Comput. Stat.* **2010**, *2*, 128–149.

[76] Lundstedt, T.; Seifert, E.; Abramo, L.; Thelin, B.; Nyström, Å.; Pettersen, J.; Bergman, R. Experimental design and optimization. *Chemom. Intell. Lab. Syst.* **1998**, *42*, 3–40.

[77] Onsekizoglu, P.; Bahceci, K. S.; Acar, J. The use of factorial design for modeling membrane distillation. *J. Membr. Sci.* **2010**, *349*, 225–230.

[78] Liu, Y. F.; Tang, X. S.; Deng, M.; Zhu, T.; Bai, Y. Z.; Qu, D. R.; Huang, X. B.; Qiu, F. One-step aqueous synthesis of highly luminescent hydrophilic AgInZnS quantum dots. *J. Lumin.* **2018**, *202*, 71–76.

[79] Bujak, P.; Wróbel, Z.; Penkala, M.; Kotwica, K.; Kmita, A.; Gajewska, M.; Ostrowski, A.; Kowalik, P.; Pron, A. Highly luminescent Ag-In-Zn-S quaternary nanocrystals: Growth mechanism and surface chemistry elucidation. *Inorg. Chem.* **2019**, *58*, 1358–1370.

[80] Sharma, D. K.; Hirata, S.; Bujak, L.; Biju, V.; Kameyama, T.; Kishi, M.; Torimoto, T.; Vacha, M. Influence of Zn on the photoluminescence of colloidal $(AgIn)_xZn_{2(1-x)}S_2$ nanocrystals. *Phys. Chem. Chem. Phys.* **2017**, *19*, 3963–3969.

[81] Yarema, O.; Yarema, M.; Wood, V. Tuning the composition of multicomponent semiconductor nanocrystals: The case of I-III-VI materials. *Chem. Mater.* **2018**, *30*, 1446–1461.